J Nanopart Res (2010) 12:2989–3002
DOI 10.1007/s11051-010-9889-2

RESEARCH PAPER

Thermo-mechanical behavior of nano aluminum particles with oxide layers during melting

Puneesh Puri · Vigor Yang

Received: 26 November 2009 / Accepted: 22 February 2010 / Published online: 12 March 2010

Abstract Molecular dynamics simulations were performed to study the thermo-mechanical behavior of nano aluminum particles coated with crystalline and amorphous oxide layers during melting. The analysis employs the Streitz–Mintmire potential, along with micro-canonical (NVE) and isobaric–isoenthalpic (NPH) ensembles. The effect of particle size in the range of 5–10 nm with oxide thickness in the range of 1–2.5 nm was investigated. The melting phenomenon was characterized using a combination of structural and thermodynamic parameters. Various fundamental processes, including structural changes, stress development, and phase transformations in both the aluminum core and the oxide shell, were examined and quantified systematically. The diffusion of aluminum cations through the oxide layer was also explored. In addition, a structural analysis was applied to determine the stress field in the oxide shell due to the volume dilatation in the aluminum core. In the particle-size range considered here, the oxide layer melts at $\sim$1,100 K, substantially lower than the value for bulk alumina (2,327 K). The oxide thickness exerts a weak influence on the melting temperature of the shell. The aluminum core melts at a temperature considerably lower than its bulk value of 940 K, a situation comparable to that of a pure nano aluminum particle. This study is an important milestone in the development of a multi-scale theory for the ignition and combustion of nano-particulate aluminum.

Keywords Aluminum · Nanoparticles · Oxide · Melting · Molecular dynamics · Modeling and simulation

Abbreviations

A, B, C	Constants used in Streitz–Mintmire potential
Al	Aluminum
Al_2O_3	Aluminum oxide
F	Energy required to embed atom in environment with given electron density
J	Second derivative associated with self-Coulomb repulsion
N_A	Avogadro's number
P	Pressure
q_i	Charges
r	Radial coordinate
r_i	Location of *i*th particle; inner radius of particle
r_o	Outer radius of particle
r_{ij}	Distance between two atoms
R_u	Universal gas constant
T	Temperature

P. Puri
The Pennsylvania State University, University Park,
PA 16802, USA
e-mail: puneesh.puri@gmail.com

V. Yang (✉)
School of Aerospace Engineering, The Georgia Institute
of Technology, Atlanta, GA 30332, USA
e-mail: vigor.yang@aerospace.gatech.edu

V	Potential
α, β, ξ	Constants used in Streitz–Mintmire potential
δ	Thickness, Lindemann index
ζ	Decay length for atomic orbital
μ	Constant used for charge evolution
v	Electrostatic interaction energy
χ	Electronegativity
λ	Translational order parameter, mean free path
φ	Pair-wise atomic interactions
ρ	Electron density
σ	Stress
Z	Core charge

Introduction

Micron-sized aluminum particles have been widely used as an ingredient in solid energetic materials because of their high energy density and low cost. The physiochemical properties of these particles have been extensively studied since the mid-1950s. In recent years, nanoscale materials and composites, characterized by ultrafine grain size, have attracted widespread interest due to their unusual energetic properties (Ilyin et al. 2001; Kwon et al. 2003). At nanoscales, particles exhibit many features distinct from their counterparts at microscales. These are associated with higher specific surface area, higher reactivity, potential ability to store energy in surface defects, lower melting points, and smaller characteristic times for mass and energy transport. This study explores some of the fundamental issues concerning the behaviors of nano-sized aluminum particles with oxide layers, with emphasis placed on their thermomechanical properties during melting.

Aluminum particles are usually covered with a passivating oxide layer (Al_2O_3) with a thickness of the order of 2–5 nm (Bucher et al. 2000), which protects the particle from further oxidation and has a significant bearing on the thermodynamic and chemical properties of the particle. When introduced into a high temperature environment, the particle melts. The phenomenon involves solid–solid phase transformations, diffusion of cations and anions, and cracking within the oxide layer. Each of these processes plays an important role in determining the characteristics of particle ignition and combustion over a broad range of scales.

Particle size, in addition to material properties and ambient conditions, dictates the physiochemical behaviors of particles in various oxidizing environments. For micron-sized and larger aluminum particles, the ignition temperature coincides with the melting point of the surface oxide layer at 2,327 K (Bucher et al. 2000). The impervious nature of aluminum oxide inhibits the ignition of aluminum. Once the layer melts, it coalesces to form an oxide cap. The aluminum core is then exposed to the ambient gases for oxidation. At nanoscales (<100 nm), ignition occurs near the melting point of aluminum at 940 K through cracking of the oxide shell, possibly caused by the pressure buildup (Rai et al. 2004) and/or phase transformations (Dreizin 1999, 2003; Trunov et al. 2006) inside the shell. Trunov et al. investigated the transformations from the amorphous to the gamma and alpha phases in the oxide layer with increase in the ambient temperature (Trunov et al. 2006). As a consequence of the density variations in different phases, the layer develops cracks. According to Rai et al. (2004), the volume dilatation due to melting of the aluminum core causes a pressure buildup inside the oxide shell. Due to the higher curvature at nanoscales as compared to micron-sized particles, the stress developed becomes unsustainable and the shell subsequently ruptures. This concept was originally introduced by Rozenband and Vaganova (1992), who developed a model taking into account the mechanical stresses at the metal–oxide interface. In the light of the inconsistency and uncertainties of existing theories concerning particle behavior during melting (Bucher et al. 2000; Rai et al. 2004; Dreizin 1999, 2003; Trunov et al. 2006; Rozenband and Vaganova 1992), fundamental research based on well-calibrated techniques appears to be imperative, to achieve improved understanding of the effects of particle size on melting and ignition behavior.

In our previous study, the melting behavior of a pure nano-aluminum particle was studied in the size range of 2–9 nm by means of molecular dynamics (MD) simulations (Puri and Yang 2007). Five different potential functions (the Lennard–Jones, Glue, embedded-atom, Streitz–Mintmire, and Sutton–Chen potentials) were implemented, and isobaric–isoenthalpic

(NPH) ensembles were used. The melting temperature of a pure nanoparticle increases monotonically with increasing size, from 473 K at 2 nm to a bulk value of 937 K at ~8 nm. Among the five potentials considered, only the many-body Glue and Streitz–Mintmire potentials accurately predicted the melting temperature as a function of particle size. A subsequent study was performed to investigate the effect of void size and pressure on the melting temperatures of bulk and nanoparticulate aluminum (Puri and Yang 2008). Alavi and Thompson (2006) performed MD simulations for clusters of pure aluminum up to 1,000 atoms, focusing on the cluster structure and dynamic coexistence of melting. Alavi et al. (2005) further explored the structure and charge distributions of bulk crystalline Al_2O_3, a surface slab of Al_2O_3, and an isolated Al_2O_3 nanoparticle. Campbell et al. (2005) simulated the oxidation of naked aluminum with a size of 20 nm.

The aforementioned studies have provided much information about the melting behavior of pure aluminum particles at nanoscales. Detailed knowledge for particles coated with oxide layers, however, is not available. This study addresses this issue based on MD simulations. The Streitz–Mintmire potential was selected due to its ability to capture the size dependence of thermodynamic properties, and to handle interactions between aluminum and oxygen atoms. This study treats a spherical aluminum core in the face-centered cubic (FCC) structure covered with an oxide shell in both amorphous and crystalline (corundum) forms, as shown in Fig. 1. Various fundamental processes involved in particle melting are explored over an appropriate range of particle size and oxide layer thickness.

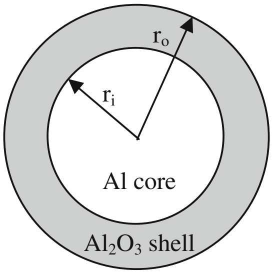

Fig. 1 Schematic of a spherical nanoparticle with aluminum core and oxide shell

Molecular dynamics simulations

The basis of this study is the general theoretical and computational framework established in our previous MD studies (Puri and Yang 2007, 2008). In short, isobaric–isoenthalpic (NPH) and micro-canonical (NVE) ensembles are employed to model the melting of bulk and nano-particulate aluminum. In NPH ensembles, a system of N atoms is coupled to an external source by introducing additional variables into the Lagrangian using volume as an extra degree of freedom through mechanical coupling (Anderson 1980). The equations of motion for NPH and NVE ensembles are numerically integrated using a fifth-order predictor–corrector and the Verlet algorithm, respectively (Allen and Tildesley 1989). These codes have been parallelized using the atomic decomposition method (Plimpton 1995). The time step is chosen to be one femtosecond, considering that the timescale associated with vibration of atoms is of the same order by magnitude. An optimum heating rate of 0.1 K per femtosecond is employed based on the trade-off between computational efficiency and resolution of calculated thermodynamic and structural properties. Through a parametric study it was found that a heating rate between 0.01 and 0.1 K per step is sufficient enough for particles to equilibrate. Annealing is achieved using velocity scaling.

The interatomic interactions are captured using the Streitz–Mintmire potential (Streitz and Mintmire 1994). This is a many-body potential consisting of an embedded-atom (V_{EAM}) and an electrostatic (V_{ES}) part. The former is defined as

$$\begin{aligned}
V_{\mathrm{EAM}} &= \sum_i F_i[\rho_i] + \sum_{i<j} \varphi_{ij}(r_{ij}) \\
\rho_i(r) &= \sum_{i \neq j} \xi_j e^{-\beta_j (r_{ij} - r_j^*)} \\
F_i(\rho_i) &= -A_i \sqrt{\frac{\rho_i}{\xi_i}} \\
\varphi_{ij}(r) &= 2B_{ij} e^{-\frac{\beta_{ij}}{2}(r - r_{ij}^*)} - C_{ij}\left[1 + \alpha(r - r_{ij}^*)\right] e^{-\alpha(r - r_{ij}^*)}.
\end{aligned} \tag{1}$$

Here, $F_i(\rho_i)$ represents the energy required to embed atom i in an environment with an electron density ρ_i, and $\varphi_{ij}(r)$ the pair-wise interaction. The functions used in the embedded-atom part of the Streitz–Mintmire potential are shown in Fig. 2. The pair potential $\varphi_{ij}(r)$ becomes strongly repulsive at a small interatomic distance. The electrostatic part accounts for electric charges on atoms, and is given by

$$\begin{aligned} V_{\mathrm{ES}} &= \sum_i v_i(q_i) + \frac{1}{2} v_{ij}(r_{ij}; q_i; q_j) \\ v_i(q_i) &= v_i(0) + \chi_i^0 q_i + \frac{1}{2} J_i^0 q_i^2 \\ v_{ij}(r_{ij}; q_i; q_j) &= \int \mathrm{d}^3 r_1 \int \mathrm{d}^3 r_2 \rho_i(r_1; q_i) \rho_j(r_2; q_j)/r_{12} \end{aligned} \tag{2}$$

where $v_i(q_i)$ is the local atomic energy, χ_i^0 is the electronegativity, J_i^0 is the second derivative associated with the self-Coulomb repulsion, and $v_{ij}(r_{ij}; q_i; q_j)$ is the electrostatic interaction energy between atoms i and j. The charge density distribution, $\rho_i(r; q_i)$, for the Slater 1s orbital about atom i for a charge q_i is defined as (Roohtan 1951)

$$\rho_i(r; q_i) = Z_i \delta(r - r_i) + (q_i - Z_i)\left(\frac{\zeta_i^3}{\pi}\right) e^{-2\zeta_i |r - r_i|} \tag{3}$$

where ζ_i is the decay length for the atomic orbital, and Z_i the effective core charge. The parameters used in the above functional forms are provided in detail in (Streitz and Mintmire 1994). The integrals in Eq. 2 can be further simplified to polynomial forms using the approach described in (Roohtan 1951). More detailed information is given in our previous MD study (Puri and Yang 2007).

Using the dynamic charge transfer, the charges q_i on each atom are calculated by minimizing the electrostatic energy (i.e., the electronegativity equalization condition), subject to the charge neutrality constraint, $\sum_i q_i = 0$ (Rappe and Goddard 1991). This yields a set of linear equations

$$\sum_j V_{ij} s_j = -\chi_i; \sum_j V_{ij} t_j = -1 \tag{4}$$

and charges are obtained using $\mu = \sum_i s_i / \sum_i t_i$ and $q_i = s_i - \mu t_i$. Due to its functional form and the way in which the various underlying parameters are defined, the Streitz–Mintmire potential can be used to treat Al–O, O–O, and Al–Al interactions.

The NVE and NPH algorithms developed in this study have been validated against argon in different phases (solid, liquid, and vapor), as well as its thermodynamic transition from the solid to the liquid phase, due to the availability of extensive and reliable experimental and numerical data (Solca et al. 1997, 1998). The cohesive energy, thermodynamic properties like bulk melting temperature, and structural properties like radial distribution function are benchmarked. The overall approach was also examined by comparing the calculated cohesive energies and melting points for both aluminum and alumina against experimental data. Figure 3 shows the calculated Al–Al, Al–O, and O–O radial distribution functions for alumina. The interatomic distances for peak values for Al–Al, Al–O, and O–O coordination are 2.9, 1.58, and 2.65 Å, respectively. Good agreement with experimental values is obtained. Figure 4 shows Al_2O_3, AlO, and Al_2O fragments coming out of a 5 nm alumina particle when heated beyond 4,000 K. The Al and O atoms in the crystal are initially packed in a hexagonal structure, equilibrated at room temperature, and then heated at 800 MPa until decomposition occurs (decomposition of alumina occurs at temperatures greater than 4,000 K). The decomposition products qualitatively validates that the SM potential can indeed simulate molecular interactions in the alumina particle. Details on the computational framework, comparison of different potentials, and validation studies for the MD code are discussed in Puri and Yang (2007).

Results and discussion

The theoretical and numerical framework summarized in the preceding section has been applied to study the particle melting behavior in the size range of 5–10 nm. The simulation commences with a spherical aluminum particle in an FCC crystal structure covered with either a crystalline or an amorphous oxide layer. The oxide thickness is 1–2.5 nm. Figure 5 shows the structures of nanoparticles under consideration at room temperature. A hexagonal crystal structure is chosen to treat crystalline Al_2O_3. In the case of an amorphous layer, the shell is preheated to a temperature higher than the melting point of Al_2O_3 (2,327 K) and cooled to room temperature.

The macroscopic thermodynamic properties are derived from the instantaneous values using the equation of state and statistical mechanics. The

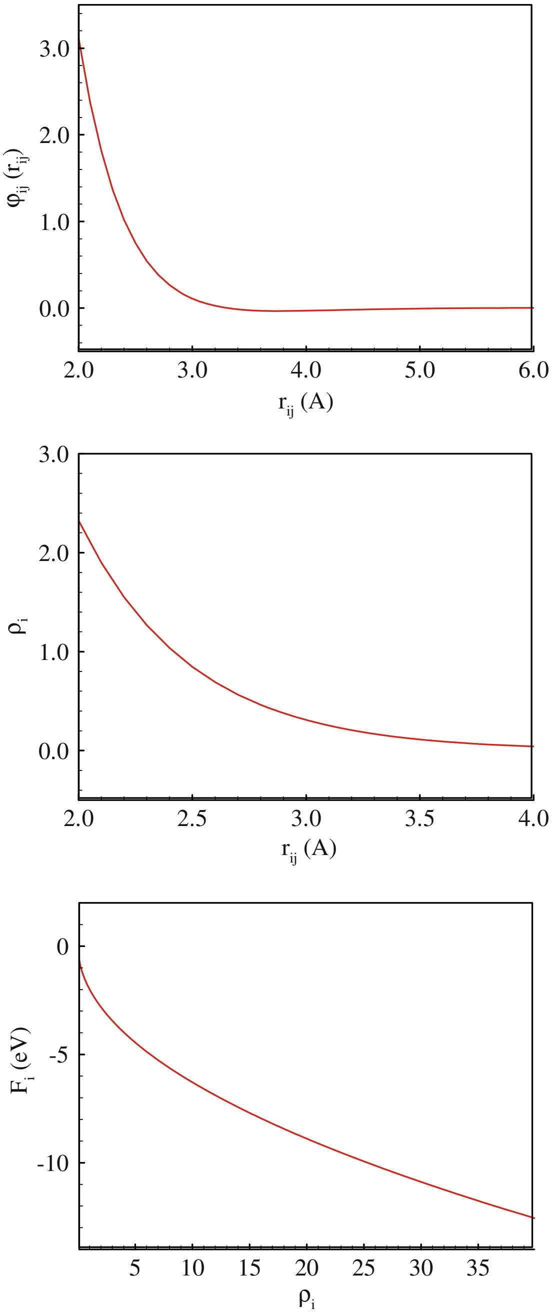

Fig. 2 Embedded-atom (EAM) part of the Streitz–Mintmire potential

Lindemann index measures the vibrational motion of particles, and is calculated as a function of the distance between atoms (Zhou et al. 2002). The Lindemann index is given by (Anderson 1980)

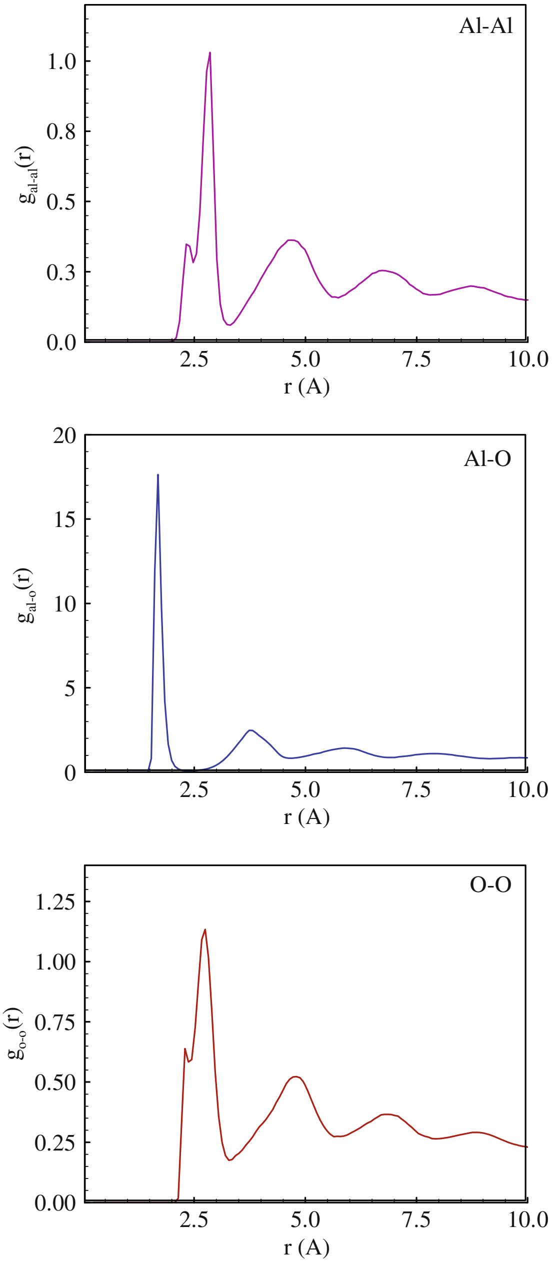

Fig. 3 Radial distribution functions for Al–Al, Al–O, and O–O interactions

$$\delta = \frac{2}{N(N-1)}\sum_{i<j}\frac{\sqrt{\left\langle r_{ij}^2\right\rangle_t - \left\langle r_{ij}\right\rangle_t^2}}{\left\langle r_{ij}\right\rangle_t}. \qquad (5)$$

The translational order parameter is indicative of the ordered structure in any phase. It has a value of approximately unity for a solid state, and drops to

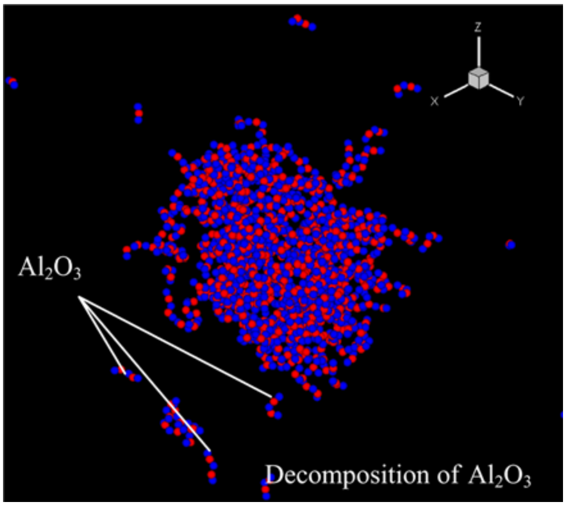

Fig. 4 Fragmentation and decomposition of Al_2O_3 from an alumina particle when heated beyond 4,000 K; initial diameter of 5 nm

nearly zero for a liquid state (Gezelter et al. 1997). It can be expressed as

$$\lambda = \frac{1}{N}\sqrt{\left(\sum_{i=1}^{N}\cos(k.r_i)\right)^2 + \left(\sum_{i=1}^{N}\sin(k.r_i)\right)^2}$$
$$k = \left(\frac{(2N)^{1/3}\pi}{L}\right)(-1,1,1), \qquad (6)$$

where k is an arbitrary vector of the lattice and L the side length of the simulation domain. A separate post-processing code was developed to superimpose the numerical grid on the geometry under consideration, and to analyze the results based on the contours of various thermodynamic properties.

The aluminum core and oxide layer are equilibrated at room temperature for a minimum of 15,000 time marching steps, using a micro-canonical ensemble. Figure 6 shows the variation of the Lindemann index during the equilibration calculation for a 5-nm particle (3 nm of core diameter and 1 nm crystalline oxide thickness). The index is initially set to zero. After a transient phase, it stabilizes at constant values of 0.028 and 0.012 for the core and oxide layer, respectively. The particle is then heated at a rate of 0.1 K per femtosecond. This procedure is adopted from similar previous studies on heating of nanoparticle after equilibration (Campbell et al. 2005; Solca et al. 1997, 1998). The numerical code has flexibility to either heat both the core and shell or heat only the oxide shell. This is to simulate experimental conditions where Al_2O_3 absorbs particular frequency of radiation more than aluminum

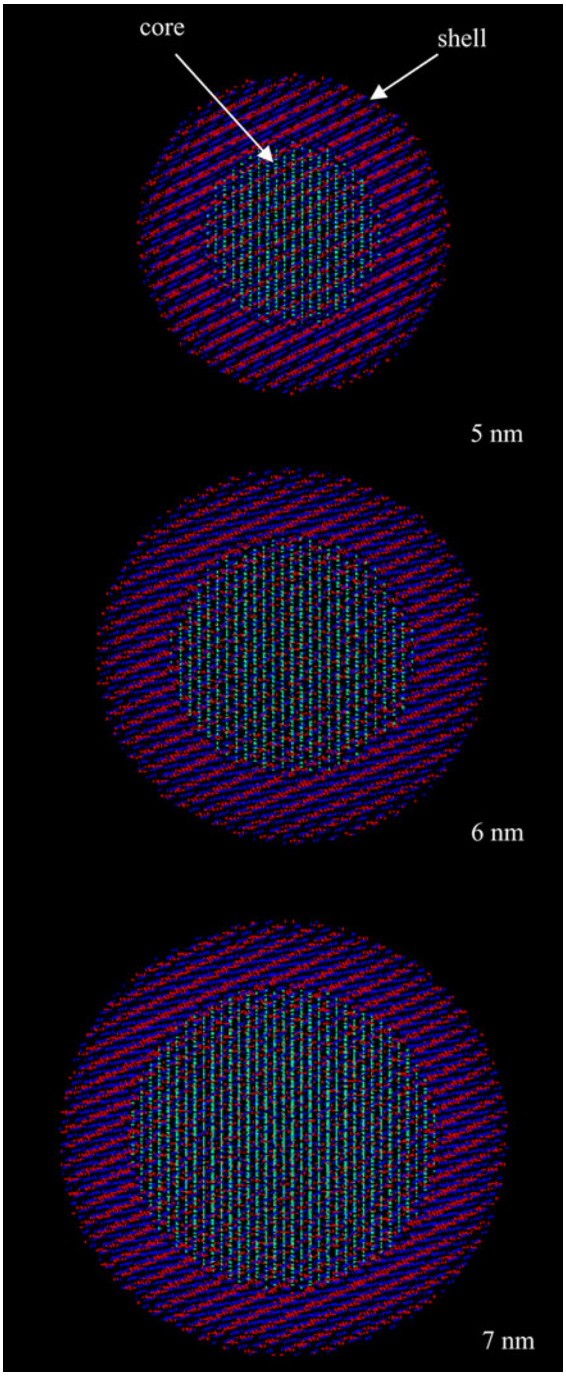

Fig. 5 Aluminum nanoparticles with crystalline oxide layer at room temperature

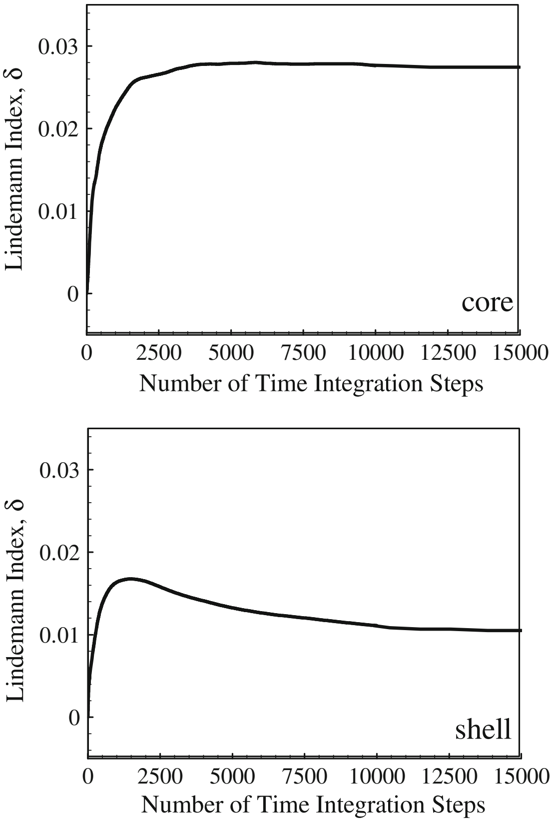

Fig. 6 Equilibration calculations for 5 nm particle (3 nm core diameter and 1 nm crystalline oxide thickness)

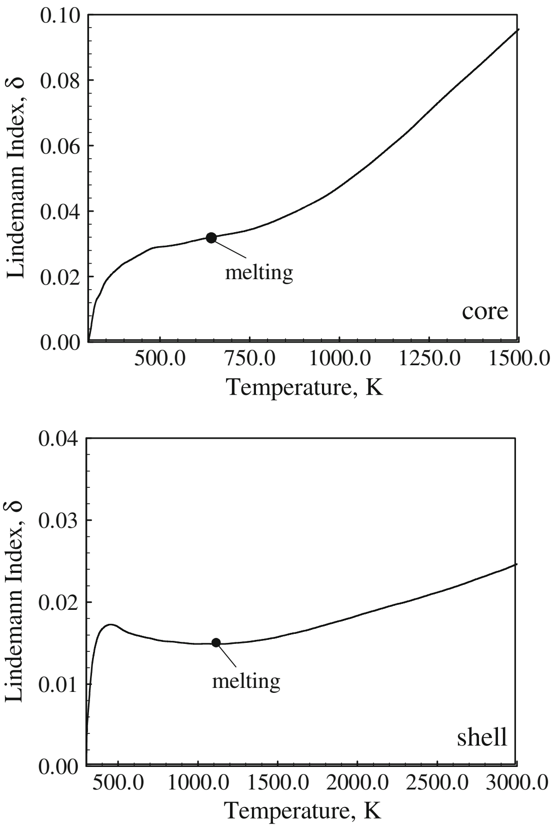

Fig. 7 Evolution of Lindemann indices for aluminum core and crystalline oxide layer; 5-nm particle (3 nm core diameter and 1 nm oxide thickness)

and can heat up frequently keeping the aluminum at same temperature.

Figure 7 shows the evolution of the Lindemann indices for both the aluminum core and oxide shell. Figure 8 shows the density contours for the particle at different temperatures. The phase transition in various stages is clearly observed. As the particle is heated, the Lindemann index for the aluminum core increases and reaches an inflection point at 0.03, at which point nucleation for the solid–liquid phase transition occurs at 650 K (see Fig. 8c). It is to be noted that characteristic increase in the Lindemann index during the melting of nanoparticles is different from sharp increases seen in bulk due to the presence of surfaces and nucleation effect seen at the femtosecond scales used in the simulations. The density of the core drops from 2,700 kg/m^3 in the solid state to 2,400 kg/m^3 in the liquid state. The method for calculating density profiles has been adopted from the study by Little et al. where the three-dimensional space is divided into small cells (bins), and particles are binned in these cells. The density is calculated as a function of number of particles in each cell (Little 1996). The Lindemann index of the oxide shell drops due to the solid–solid phase transition, after an initial increase to a peak value of 0.018 at 500 K during the transient phase.

Alumina is known to exist in six different polymorphs (corundum, Rh_2O_3, *Pbnm* perovskite, *R3c*-perovskite, *A*-type rare earth sesquioxide, and *B*-type rare earth sesquioxide; Duan et al. 1998). Due to the high interfacial stress and hence pressure, the initial structure studied here is corundum, which transforms to one of the other five denser polymorphs. The contour plot at 550 K, shown in Fig. 8b, indicates a density change from 3,890 to 4,050 kg/m^3 as a result of such a phase transition. In the crystalline structure of Al_2O_3, aluminum atoms occupy tetrahedral or octahedral voids in the lattice formed by

Fig. 8 Density distributions at various temperatures during heating of 5-nm particle. **a** Initial state, **b** solid-solid phase transition in Al_2O_3, **c** solid–liquid phase transition in Al, **d** solid–liquid phase transition in Al_2O_3

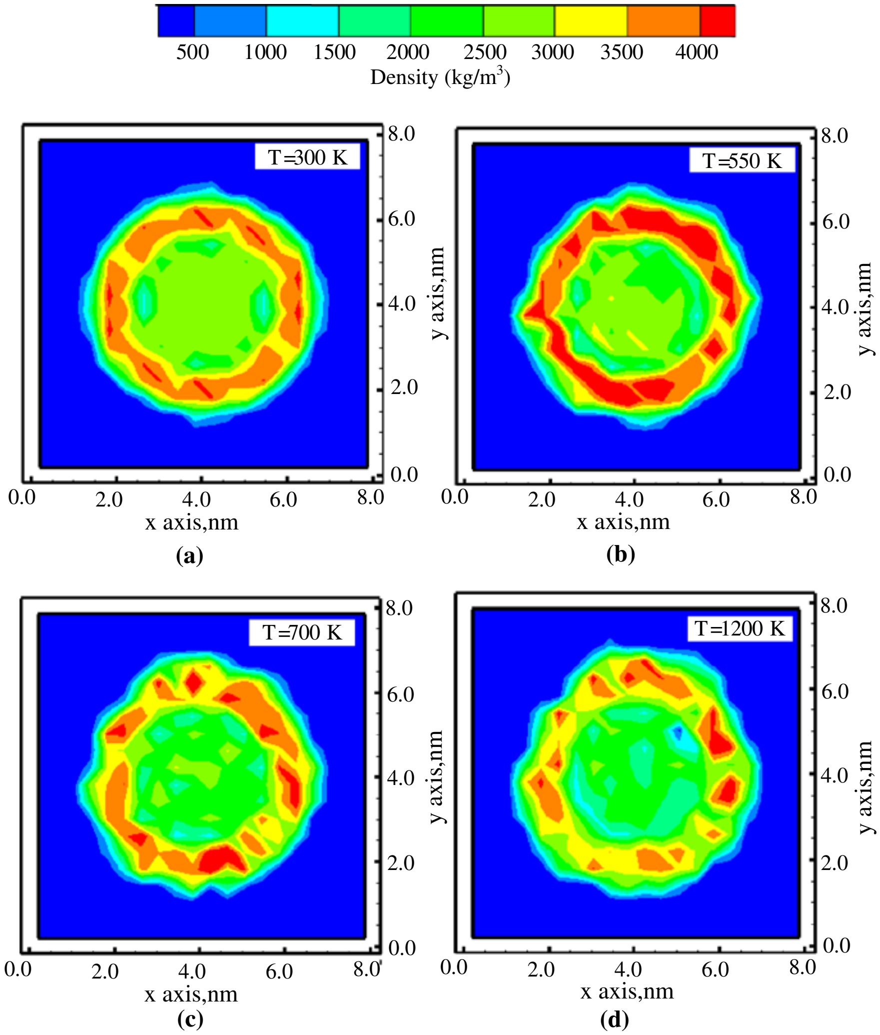

oxygen atoms. When these aluminum atoms change their coordination from six to a higher value, a solid–solid transition to a denser crystalline structure occurs (Duan et al. 1998). As the temperature continues to increase, the shell melts at 1,129 K, where the inflection point appears in the Lindemann index profile. The situation is similar to that for the aluminum core. The density of the oxide shell decreases to 3,010 kg/m^3 in the liquid state, as shown in Fig. 8d.

The size dependence of the melting phenomenon is examined in the range of 5–10 nm. In each case, the thickness of the oxide layer remains at 1 nm. Figure 9 shows the evolution of the Lindemann indices for the aluminum core and oxide shell as a function of temperature. The core melts at a temperature considerably lower than its bulk value of 940 K. The oxide layer melts at 1047, 1100, and 1159 K, respectively, for particle sizes of 6, 7, and 8 nm. Nucleation of the liquid phase takes place at relatively lower temperatures of 986 and 1,008 K for 9 and 10 nm particles. These temperatures are substantially lower than the counterpart for bulk alumina, which is 2,327 K. The size dependence of the melting behavior for pure aluminum was reported in our previous study (Puri and Yang 2007). The results from this study indicate an identical trend for both the aluminum core and oxide shell. This phenomenon can be attributed to the increase in the specific surface area as the particle size decreases.

The effect of the oxide shell thickness on particle melting is explored in the range of 1.0–2.5 nm. The

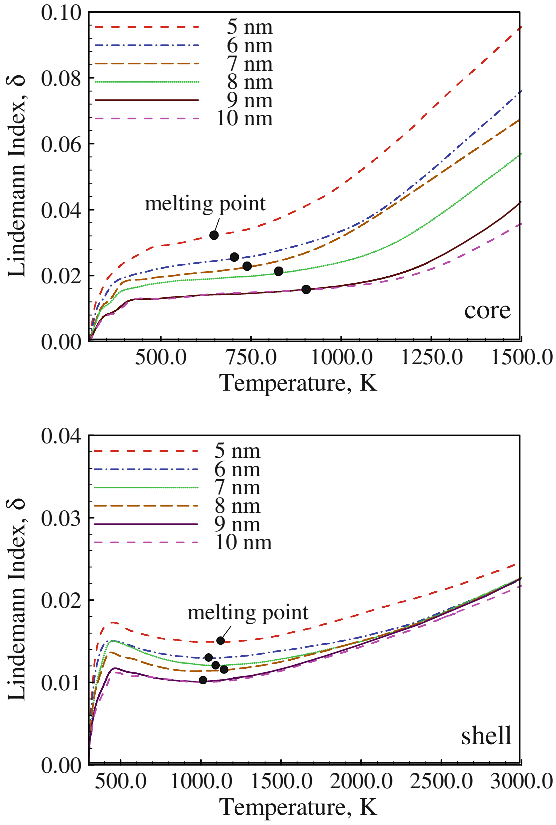

Fig. 9 Evolution of Lindemann indices for aluminum core and crystalline oxide layer; particle size of 5–10 nm (3–8 nm core diameter and 1.0 oxide thickness)

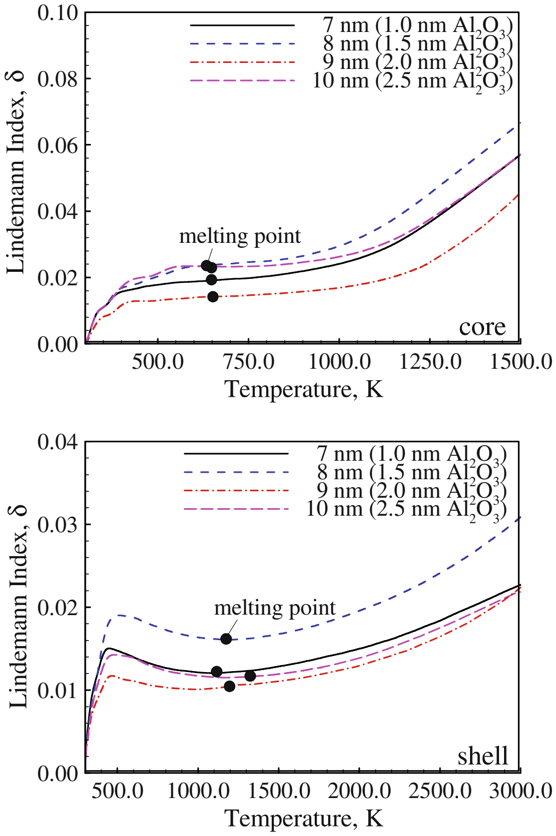

Fig. 10 Evolution of Lindemann indices for aluminum core and crystalline oxide layer; particle size 7–10 nm (5 nm core diameter and 1.0–2.5 nm oxide thickness)

core diameter is fixed at 5 nm. Figure 10 shows the evolution of the Lindemann index. The melting point of the oxide layer increases, from 1,130 K for 1.0 nm to 1,313 K for 2.5 nm thickness. The overall melting temperature results are summarized in Fig. 11.

To further understand the size dependence of alumina melting, a simulation was performed for a pure alumina nanoparticle with a diameter of 5 nm. The evolution of the Lindemann index shown in Fig. 12 indicates a melting temperature of 1,284 K. This value is consistent with that of alumina with an embedded aluminum core, which falls in the range of 986–1,313 K. The Lindemann index also bears a close resemblance to the case with an aluminum core. It increases rapidly in an initial transient phase, reaches a peak at 0.025, and then decreases, due to the phase transformation to a denser phase. The inflection point at 1,284 K marks the transition from the solid to the liquid state.

In addition to the crystalline structure, the situation with an amorphous oxide layer was investigated. To accomplish this, the crystalline structure was heated to a temperature greater than its melting point and then rapidly cooled to 300 K to obtain an amorphous layer. The resulting nanoparticle was heated afterward to allow examination of its thermo-mechanical behavior during the melting process. Figure 13 shows the evolution of the Lindemann indices for a 5-nm particle covered with either a crystalline or an amorphous oxide layer. The core melts at almost the same temperature for both cases. The sharp variation of the Lindemann index for the crystalline structure, however, is not observed in the case with the amorphous shell. For a change to the beta or the gamma form, a minimum of 4 nm thick amorphous layer would be required (Trunov et al. 2005). Since this study only considers oxide layers up to 2.5 nm thick, the transformation from the amorphous to the

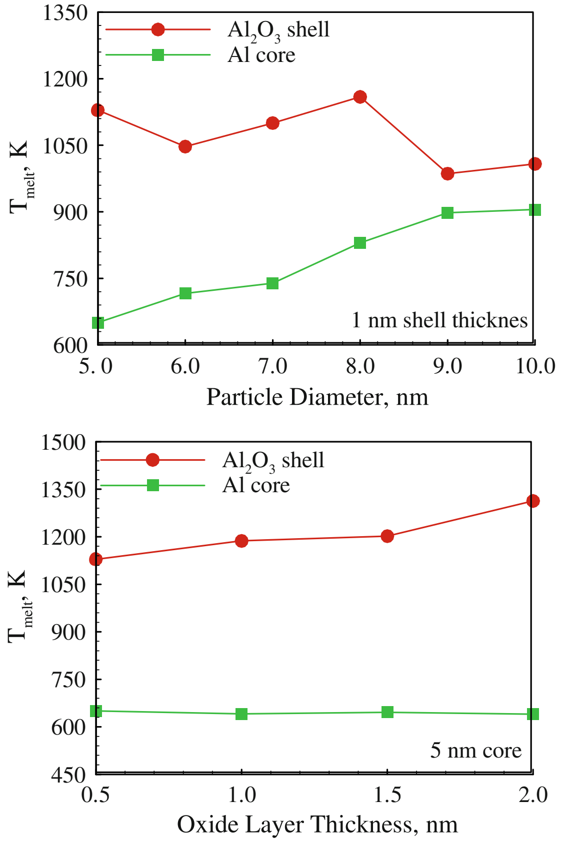

Fig. 11 Variation of melting points as function of core size and oxide layer thickness

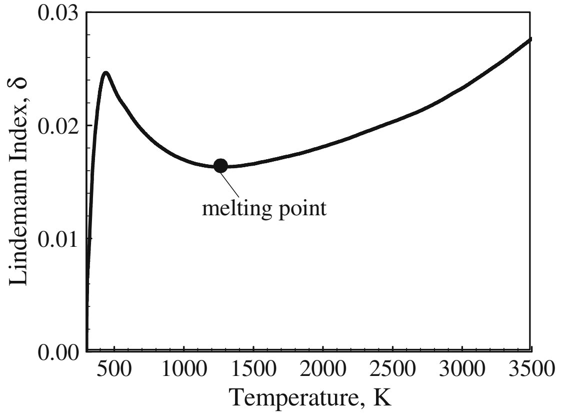

Fig. 12 Evolution of Lindemann index during heating of 5-nm pure crystalline alumina particle

gamma phase does not take place. The solid-to-liquid phase change is also absent in the case of the amorphous oxide shell.

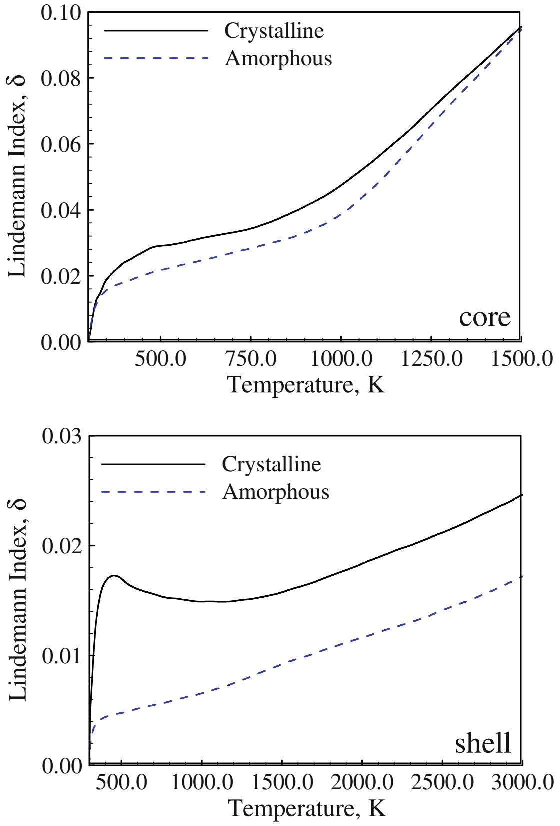

Fig. 13 Evolution of Lindemann indices during heating of 5-nm particles with crystalline and amorphous oxide layers (3 nm core diameter and 1 nm oxide thickness)

During the particle melting, the density of the aluminum core decreases from 2,700 to 2,400 kg/m^3, an 11.1% change. The associated volume dilatation exerts a significant influence on the stress development in the oxide shell. The whole process can be theoretically treated as pressure buildup in a spherical shell. For the aluminum core, the bulk modulus K is 76 GPa. The pressure developed inside the shell becomes 8.4 GPa, based on the relation $K = -\rho \partial p / \partial p$. Following basic theories in solid mechanics, the stresses in spherical coordinates under an equilibrium condition can be obtained from the following equation (Ragab and Bayouni 1999)

$$\sigma_r = p_i \left(\frac{r^3 - r_o^3}{r^3} \right) \left(\frac{r_i^3}{r_o^3 - r_i^3} \right) \quad \text{and} \\ \sigma_\theta = \sigma_\phi = p_i \left(1 + \frac{r_o^3}{2r^3} \right) \left(\frac{r_i^3}{r_o^3 - r_i^3} \right) \tag{7}$$

Table 1 Stresses developed inside the oxide shell due to melting

Core diameter (nm)	Oxide thickness (nm)	Particle diameter (nm)	$\sigma_\theta, \sigma_\phi$(GPa)	σ_r(GPa)
4.0	1.0	6.0	9.505	8.4
5.0	1.0	7.0	11.424	8.4
5.0	1.5	8.0	8.269	8.4
5.0	2.0	9.0	6.807	8.4
5.0	2.5	10.0	6.000	8.4
6.0	1.0	8.0	13.394	8.4
7.0	1.0	9.0	15.396	8.4
8.0	1.0	10.0	17.419	8.4

where p_i is the pressure exerted on the shell due to the volume expansion of the core, r the radial coordinate, and σ_r, σ_θ, σ_ϕ the stresses in the radial, azimuthal, and polar directions, respectively. The subscripts i and o denote the inner and outer radii of the oxide shell, respectively, as illustrated in Fig. 1. The maximum stress occurs at the interface. Table 1 lists the stress values for different particle sizes. The tensile strength of alumina is 0.2552 GPa at room temperature and decreases by an order of magnitude when the temperature exceeds 1,300 K (Shackelford and Alexander 2000). Since the stresses in the shell caused by the core melting are an order of magnitude higher than the tensile strength, the shell should crack. In this MD study, however, the shell remains intact. This may be attributed to the fact that the rate of the solid-to-liquid phase transition in the shell is too fast to allow for any substantial stress development in the solid phase.

Several experimental studies on aluminum substrates and films have revealed that when an aluminum particle coated with an oxide layer is heated from room temperature, the oxide layer grows due to diffusion of aluminum cations through the layer and bonding with oxygen atoms at the surface (Jeurgens et al. 2002). It is instructive to consider whether a similar phenomenon occurs for nanoparticles in the present research. Before heating, the core consists of aluminum atoms arranged in an FCC structure, and the shell contains Al_2O_3 atoms arranged in a hexagonal structure. The phenomenon of diffusion of aluminum cations for cases with different shell thicknesses is shown in Fig. 14. This shows snapshots of particle structures with crystalline shells. The core diameter is fixed at 5 nm, and the shell thickness varies from 1 to 2 nm. The diffusion of aluminum cations through the shell is evident, especially for smaller particles. For an amorphous shell, the diffusion of cations proceeds much faster, as shown in Fig. 15. The potential gradient caused by the positive and negative charges gives rise to the movement of cations and the ensuing growth of the shell. Once the charge gradient is nullified due to the diminished diffusion of cations, the shell stops growing. This commonly happens when the shell thickness reaches 5 nm, a typical oxide layer thickness reported in the literature (Jeurgens et al. 2002). The characteristic timescales of diffusion and melting (which leads to cracking) are strong functions of pressure, temperature, size of core and oxide thickness. The relative variation of these parameters determines the prominent mode of either cracking of oxide or oxidation through diffusion of ions. Since this study focuses on thermo-mechanical behavior, all the simulations were carried out for nanoparticles in a vacuum. A subsequent study explores different modes of ignition based on the effect of pressure, temperature, oxidizer, oxide thickness, and particle diameter and is investigated using time and length scales involved during ignition and combustion (Puri and Yang 2009). If the particles were exposed to oxygen, these aluminum cations would combine to form species like AlO, Al_2O, which would then deposit on the surface and increase the oxide thickness.

The failure mechanism is most often associated with the imperfections in the crystal structure or interfaces present within the sample. The scale of such imperfections or interfaces would be comparable to the scale of the entire particle (or shell) under consideration in this article. One obvious interface in the present system is between the core and shell, and its mechanical properties are of great significance.

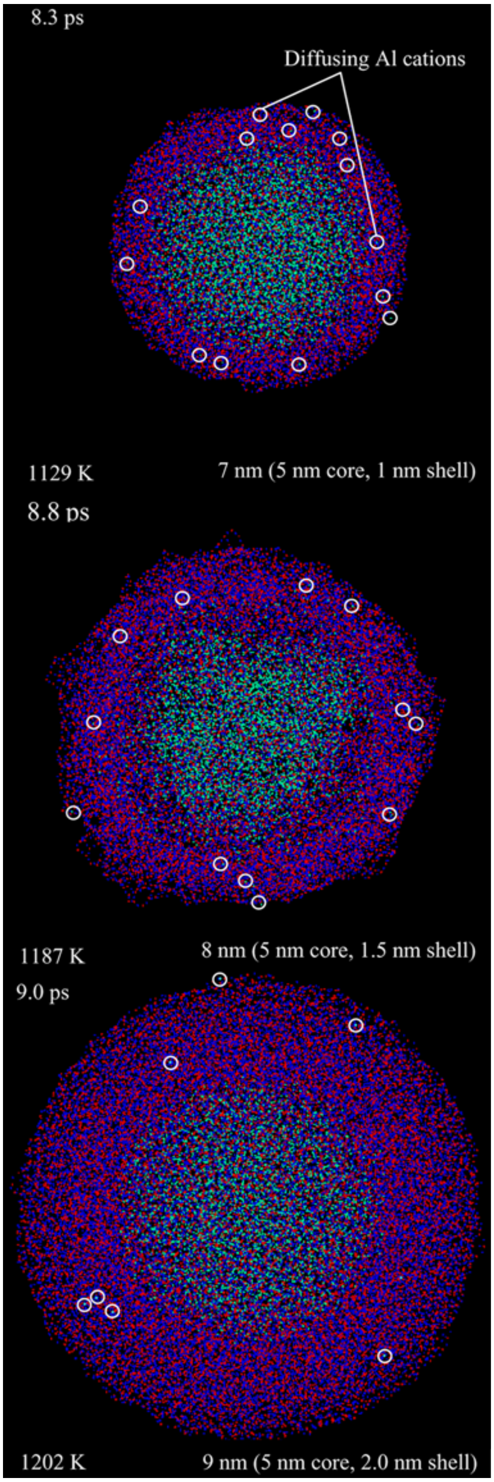

Fig. 14 Snapshots of 7–9 nm nano aluminum particles with crystalline oxide layer, showing diffusion of aluminum cations (core size of 5 nm and oxide thickness of 1–2 nm)

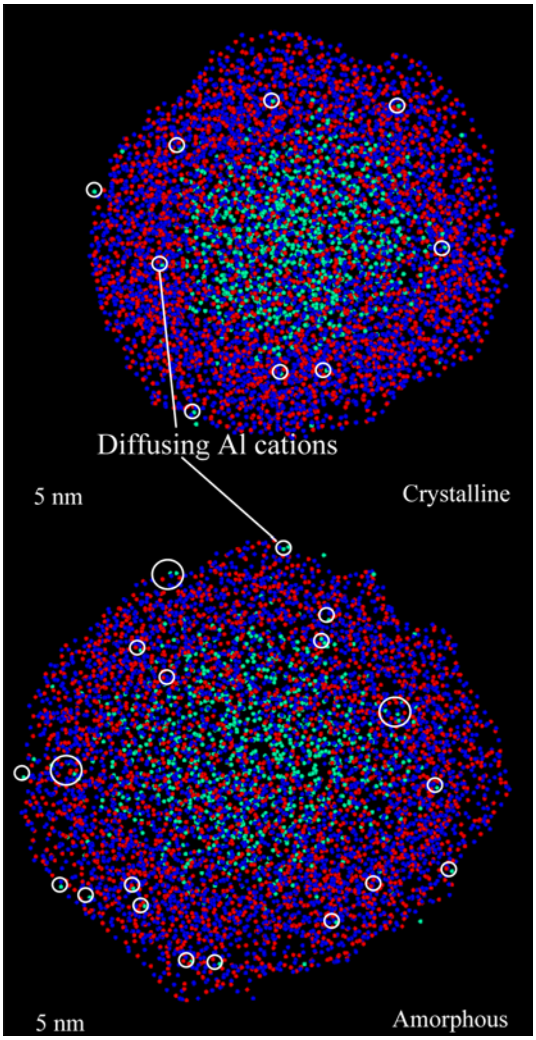

Fig. 15 Snapshot showing diffusion of aluminum cations in crystalline and amorphous oxide layers for 5-nm particle (core size of 5 nm and oxide thickness of 1 nm)

Thus, as a part of subsequent study, it is important to establish the molecular mechanisms for mechanical failure in such systems using the preliminary results of this study. In that sense, the general approach of molecular dynamics appears to be highly beneficial.

Summary and conclusions

A molecular dynamics study was performed to examine the thermo-mechanical behavior of nano-aluminum particles coated with oxide layers in both the crystalline and amorphous forms. The size dependence of the melting phenomenon was first examined for particles in the range of 5–10 nm, with the oxide thickness fixed at 1 nm. In each case, the oxide layer melted at 986–1,159 K, substantially lower than the bulk value melting point of 2,327 K. The effect of the oxide shell thickness was explored in the range of 1.0–2.5 nm, with the core diameter fixed at 5 nm. The melting point of the oxide layer increased from 1,130 K for 1.0 nm to 1,313 K for 2.5 nm thickness. The results were compared with the case of a pure 5-nm alumina nanoparticle, for which melting was observed at 1,284 K. The Lindemann index curve showed qualitatively the same trend as that seen for the oxide layer with an aluminum core.

For a crystalline oxide layer, melting was preceded by a solid–solid phase transition to a denser polymorph, characterized by a decrease in the Lindemann index, as the particle was heated. This phenomenon, however, was absent in the case of amorphous layers. A structural analysis indicated that the stresses in the shell, caused by the volume dilatation in the aluminum core during melting, were an order of magnitude higher than the tensile strength. The shell may therefore crack if it melts at a rate slow enough to allow stress development in the solid phase. Diffusion of aluminum cations through the oxide shell was also investigated.

This study has shed much insight into the various thermo-physical processes involved in the melting of nano-aluminum particles. The results provide a basis for the development of a multiscale theory for the ignition and combustion of nano-particulate aluminum.

Acknowledgments This study was sponsored by the U.S. Army Research Office under the Multi-University Research *Initiative* under Contract No. W911NF-04-1-0178. The support and encouragement provided by Dr. Ralph Anthenien are gratefully acknowledged.

References

Alavi S, Thompson DL (2006) Molecular dynamics simulations of melting of aluminum nanoparticles. J Phys Chem A 110:1518–1523

Alavi S, Mintmire JW, Thompson DL (2005) Molecular dynamics simulations of oxidation of aluminum nanoparticles. J Phys Chem B 109:209–214

Allen MP, Tildesley DJ (1989) Computer simulation of liquids. Oxford Science, Oxford

Anderson HC (1980) Molecular dynamics simulations at constant pressure and/or temperature. J Chem Phys 72:2384–2393

Bucher P, Yetter RA, Dryer FL, Vicenzi EP, Parr TP, Hanson DM (2000) Detailed studies on the flame structure of aluminum particle combustion. In: Yang V, Brill TB, Ren WZ (eds) Solid propellant chemistry, combustion and motor interior ballistics. Progress in Astronautics and Aeronautics, vol 185. AIAA, Reston, VA, p 689

Campbell TJ, Aral G, Ogata S, Kalia RK, Nakano A, Vashishta P (2005) Oxidation of aluminum nanoclusters. Phys Rev B 71:205413

Dreizin EL (1999) Experimental study of aluminum particle flame evolution in normal and micro-gravity. Combust Flame 116:323–333

Dreizin EL (2003) Effect of phase changes on metal particle combustion processes. Combust Explos Shock Waves 39:681–693

Duan W, Wentzcovitch RM, Thomson T (1998) First principles study of high pressure alumina polymorphs. Phys Rev B 57:10363

Gezelter JD, Rabani E, Berne BJ (1997) Can imaginary instantaneous normal mode frequencies predict barriers to self-diffusion? J Chem Phys 107:4618–4627

Ilyin AP, Gromov AA, Vereshchagin VI, Popenko EM, Surgin VA, Lehn H (2001) Combustion of agglomerated ultrafine aluminum powders in air. Combust Explos Shock Waves 37:664–669

Jeurgens LPH, Sloof WG, Tichelaar FD, Mittemeijer EJ (2002) Growth kinetics and mechanisms of aluminum-oxide films formed by thermal oxidation of aluminum. J Appl Phys 92:1649–1656

Kwon YS, Gromov AA, Ilyin AP, Popenko EM, Rim GH (2003) The mechanism of combustion of superfine aluminum powders. Combust Flame 133:385–391

Little JK (1996) Simulation of droplet evaporation in supercritical environments using parallel molecular dynamics, Ph.D. Dissertation, Penn State

Plimpton S (1995) Fast parallel algorithms for short range molecular dynamics. J Comput Phys 117:1–19

Puri P, Yang V (2007) Effect of particle size on melting of aluminum at nano scales. J Phys Chem C 111:11776–11783

Puri P, Yang V (2008) Molecular dynamics simulations of effects of pressure and void size on melting of aluminum. J Nanopart Res 11:1117–1127

Puri P, Yang V (2009) A multi-scale theory of ignition and combustion of particulate aluminum. Combust Flame (submitted)

Ragab A, Bayouni SE (1999) Engineering solid mechanics fundamentals and applications. CRC Press, New York

Rai A, Lee D, Park K, Zachariah MR (2004) Size-resolved kinetic measurements of aluminum nanoparticle oxidation with single particle mass spectrometry. J Phys Chem B 108:14793–14795

Rappe AK, Goddard WA (1991) Charge equilibration for molecular dynamics simulations. J Phys Chem 95:3358–3363

Roohtan CCJ (1951) A study of two-center integrals useful in calculations on molecular structure I. J Chem Phys 19:1445–1458

Rozenband VI, Vaganova NI (1992) A strength model of heterogeneous ignition of metal particles. Combust Flame 88:113–118

Shackelford JF, Alexander W (2000) CRC materials science and engineering handbook. CRC Press, Boca Raton

Solca J, Anthony JD, Steinebrunner G, Kircher B, Huber H (1997) Melting curves for argon calculated from pure theory. J Chem Phys 224:253–261

Solca J, Dyson AJ, Steinebrunner G, Kirchner B, Huber H (1998) Melting curves for neon calculated from pure theory. J Chem Phys 108:4107–4111

Streitz FH, Mintmire JW (1994) Electrostatic potentials for metal-oxide surfaces and interfaces. Phys Rev B 50:11996–12003

Trunov MA, Schoenitz M, Zhu X, Dreizin EL (2005) Effect of polymorphic phase transformations in Al_2O_3 film on oxidation kinetics of aluminum powders. Combust Flame 140:310–318

Trunov MA, Schoenitz M, Dreizin EL (2006) Effect of polymorphic phase transformations in alumina layer on ignition of aluminium particles. Combust Theo Model 10:603–624

Zhou Y, Karplus M, Ball KD, Berry RS (2002) The distance fluctuation criterion for melting: comparison of square well and more potential modes for clusters and homo polymers. J Chem Phys 116:2323–2329